Supplementary information to ‘Deformation of the lowermost mantle from seismic anisotropy’

Andy Nowacki[1], James Wookey[1] & J-Michael Kendall[1]

[1] *Department of Earth Sciences, University of Bristol, Wills Memorial Building, Queen’s Road, Bristol, BS8 1RJ, UK*

Supplementary Results and Discussion

SKS splitting measurements In order to estimate UM anisotropy beneath the Aleutian arc, we make new measurements of SKS splitting at stations in the AK network along similar backazimuths to the S and ScS phases studied. These are presented in Supplementary Table 1 and shown in Supplementary Fig. 10. Where more than one very good measurement was made, the error surfaces were stacked to improve the estimate of UM splitting. These are listed in Supplementary Table 2. The measurements show a clear trench-parallel trend for most of the arc, with the easternmost measurements becoming less so where a larger strike-slip component in the subduction is apparent (Supplementary Fig. 10). For stations where SKS measurements were not possible within our requirements, we check that the splitting in the S phase (after correction for source anisotropy determined using stations with reliable SKS measurements) agrees with SKS results nearby.

Dataset and results In addition to the measurements made of S–ScS differential splitting made beneath the Caribbean, a further 71 measurements of S–ScS splitting were obtained using an earthquake on the Mid Atlantic Ridge (MAR) at a focal depth of 8 km. Further examples are shown in Supplementary Fig. 13. Measured on USArray stations, these raypaths cross 16 results in D$''$ below the northeast Caribbean along an azimuth of $\sim$300°, in a region of the lowermost mantle (‘E’) $\sim$200 km square, 200 km east of that beneath Florida (Fig. 2). Stacking the error surfaces of the two sets of results[1,2] significantly removes ambiguity of the measurement and leads to improved results, which are listed in Supplementary Table 3 and shown in Fig. 2. The errors in ϕ are dominated by the variation in azimuth, and are expressed as the 95% confidence interval, as is the case for δt. Combining the two sets for a simple case of tilted transverse isotropy (TTI), the common plane normal to the rotational axis of symmetry (the 'plane of isotropy'), dips $(50 \pm 2)^\circ$ to the south (strike 091 ± 1). Errors in the plane are given to one standard deviation.

Three shallow earthquakes in Hawaii, Panama and near the Guatemalan coast recorded on stations in eastern North America and Alaska provide 28 measurements in a region ('W') $\sim$400 km square in D$''$ beneath the west-central United States (Fig. 2). Three other earthquakes (epicentral distances 87–104°) with similar backazimuths to the Central American events were used to make SKS measurements for 10 stations (see Supplementary Methods; Supplementary Table 1) in Alaska on the Aleutian arc. These and published SKS measurements are used as corrections for stations in northeast North America. This constrains the receiver-side UM contribution to the total splitting for these stations, and thus the source-side UM splitting, in S. Correcting for both and stacking the δt–ϕ error surfaces, splitting parameters in D$''$ along Central-North America raypaths are shown in Supplementary Table 4. Combining the two azimuths gives the common plane normal to the TI rotational symmetry axis ('plane of isotropy') as dipping $(30 \pm 1)^\circ$ southwest (strike 225 ± 1).

A region ('S') $\sim$600 km square beneath the Yucatan peninsula is traversed by raypaths from South America to eastern USA (191 measurements), and these are crossed by those from and East Pacific Rise (EPR) earthquakes to northeast North American stations (7 measurements) (Fig. 2; Supplementary Table 4). The combined best-fitting plane of isotropy dips southeast by $(52 \pm 2)^\circ$ (strike 056 ± 1).

These best-fitting planes are shown in Supplementary Fig. 2. Also shown are the approximate regions of ScS sensitivity in D$''$, according to ref. [3]. This shows that the most likely region from which the majority of the splitting in ScS in D$''$ is where the different azimuths overlap. Otherwise, the majority of the splitting must have occurred in the small, non-overlapping regions, which is unintuitive if we must assume that the total splitting is path-integrated in D$''$.

Variation within stacks As Supplementary Fig. 1 shows, there is some small variability of ϕ' and δt within the measurements in the paths (Supplementary Table 4). Supplementary Fig. 11 shows polar histograms in 15° bins for ϕ' along each path. The EPR–North America leg of region S shows very steep fast orientations ($\phi' \approx -10°$). This is because the three measurements from event 2008-262 are near-null, giving larger uncertainties and results which the analysis places near to the null direction. Stacking the λ_2 surfaces for these alongside the other events leads to a better-constrained result, as the fast direction in D$''$ is not as close to the source polarisation when projected into the ray frame.

$MgSiO_3$-perovskite and (Mg,Fe)O It seems very likely that $MgSiO_3$-post-perovskite (ppv) is the dominant mineral phase at D$''$ conditions, especially for realistic mantle compositions in terms of Fe and Al (ref. [4]), hence we believe that anisotropy in aligned ppv is probably the likeliest explanation for the observed shear wave splitting. However, (Mg,Fe)O is also highly anisotropic, and maybe mechanically weaker than ppv[5–8]. Hence it may be the case that MgO dominates the deformation at high strain and may align more than ppv. We test the fit of candidate shear planes and slip directions believed to dominate in MgO (ref. [8]) to our measurements of shear wave splitting as explained in the Methods section (Supplementary Fig. 12). In this case, we do not show the degree of scaling of elastic constants with colour, though the plots are otherwise the same as Fig. 3. Because of MgO's high, cubic symmetry, many planes are compatible with our measurements for some of the regions. We notice, however, that in region S in particular, there are few shallow-dipping shear planes associated with near-horizontal slip, which seems to be unlikely over a broad scale beneath downwelling. Instead, most planes and slip directions are steeper than for some of the ppv slip systems (Fig. 3).

Although unlikely to be present, we also show a high-temperature case for $MgSiO_3$-perovskite (pv) (ref. [9]). If pv is the dominant phase in any of the regions, it is likely to be so because the local temperature is too high for ppv to be present, hence using a case where T=3500 K. In regions E and W, the shear planes and slip directions must be near vertical to fit observations, and in region S it is not sufficiently anisotropic to produce the observed splitting. Hence it appears a very poor candidate for producing the measured anisotropy in D$''$.

Supplementary Figures

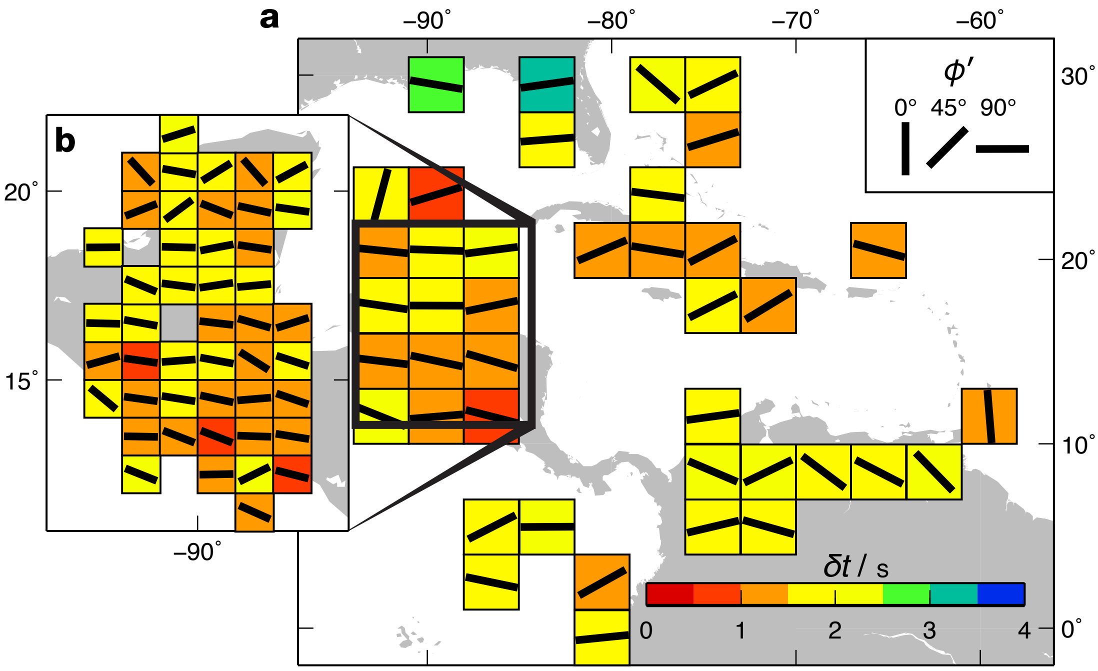

Supplementary Figure 1: Measurements of shear wave splitting from one azimuth. **a,** Results of binning measurements of ϕ' (thick black lines; angle corresponds directly to ϕ') and δt (colour as per scale) by ScS CMB bounce point into three-degree blocks (∼150 km at CMB) in the Caribbean, using deep-focus earthquakes in South America. ScS samples D″ from only one azimuth in this case. **b,** Enlargement of region beneath Yucatan peninsula binned in one degree blocks (∼50 km at CMB). The zone of sensitivity of ScS at the CMB is less than 10° perpendicular to its propagation direction (∼east-west here).

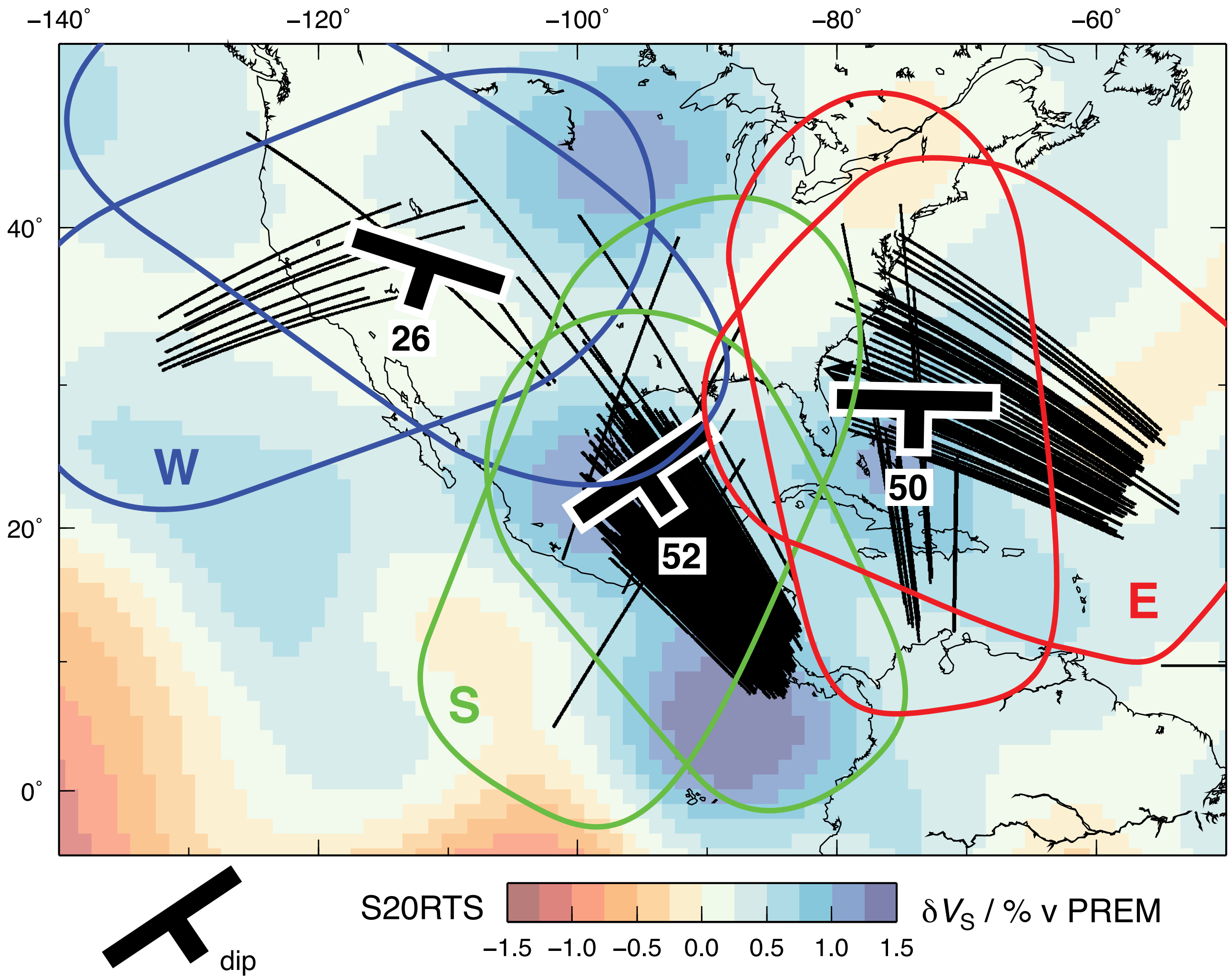

Supplementary Figure 2: Paths in D″ of ScS rays and best-fitting TTI symmetry planes. Shown are ray paths of ScS in D″, assuming it to be uniformly 250 km thick (thin black lines); orientations of best fitting planes normal to axis of rotational symmetry for TTI case of anisotropy (strike and dip symbols); zones of sensitivity of ScS in D″ for each of the sets of crossing paths in the three regions (blue, green and red outlines for ‘W’, ‘S’ and ‘E’ regions respectively). It can be seen that there is considerable overlap in the crossing rays, hence the majority of the signal we observe in the two directions is likely to come from the same area for each region. Plotted beneath is the shear velocity in D″ in the S20RTS model. See Fig. 2 for details.

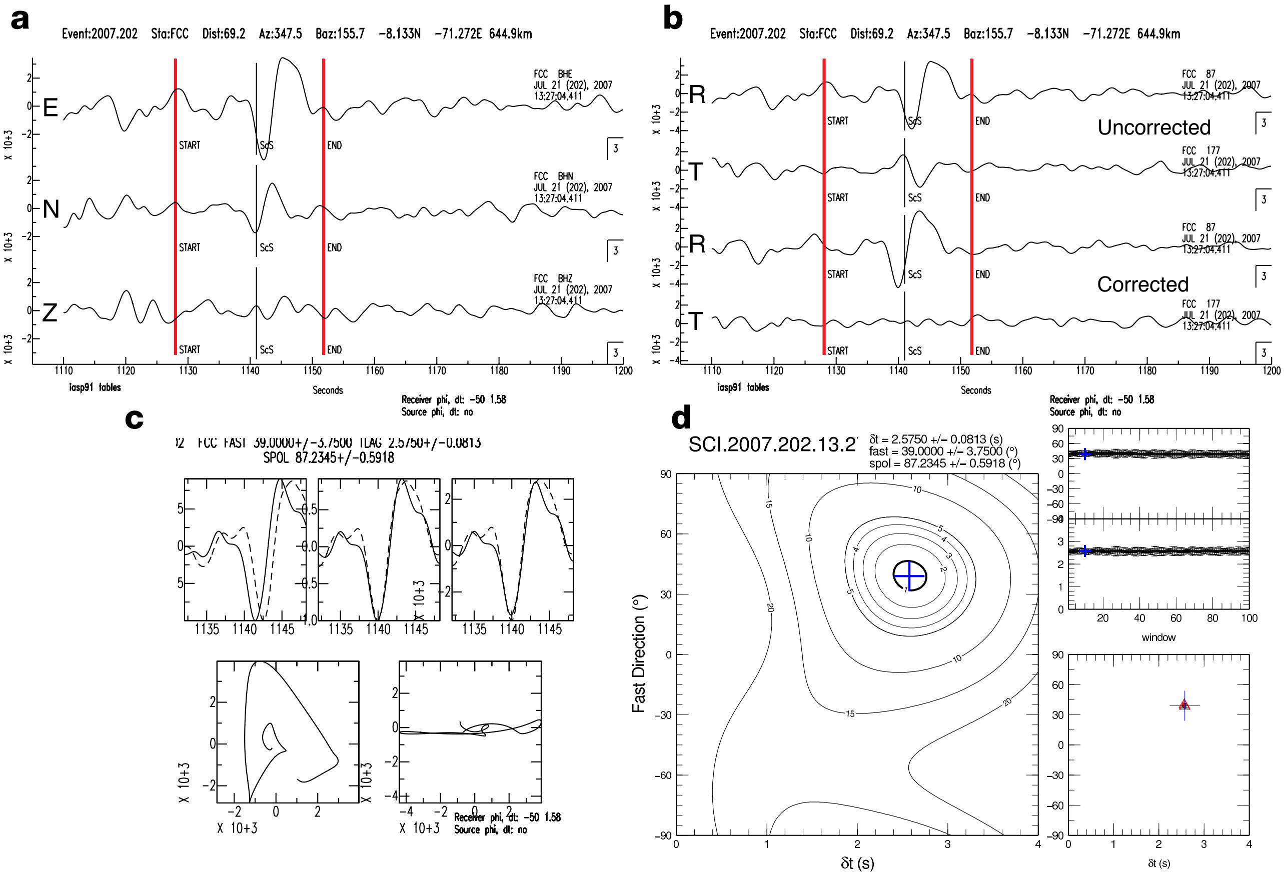

Supplementary Figure 3: Splitting analysis of ScS phase at station FCC (Fort Churchill, Canada) for a deep event (2007-202-1327, Brazil, depth 645 km). (The waveforms are displayed with a bandpass filter at 0.01–0.2 Hz for clarity of inspection, but the broadband signal is used in the analyses. The same result is found in the case of either filter.) **a,** Uncorrected east, north and vertical components of seismogram. Start and end of analysis window giving best linearisation of particle motion are indicated by red vertical lines. **b,** Uncorrected (top) and corrected (bottom) radial and transverse components. **c,** Uncorrected (top left) and corrected (top right) fast (solid) and slow (dashed) waves after rotation to the fast direction. Beneath are uncorrected (bottom left) and corrected (bottom right) horizontal particle motion. **d,** Contour surface of λ_2 (left), with the 95% confidence limit shown by thicker contour. Blue cross is the minimum λ_2, corresponding to the values of ϕ and δt which best linearise the particle motion. Right hand panels show result of cluster analysis.

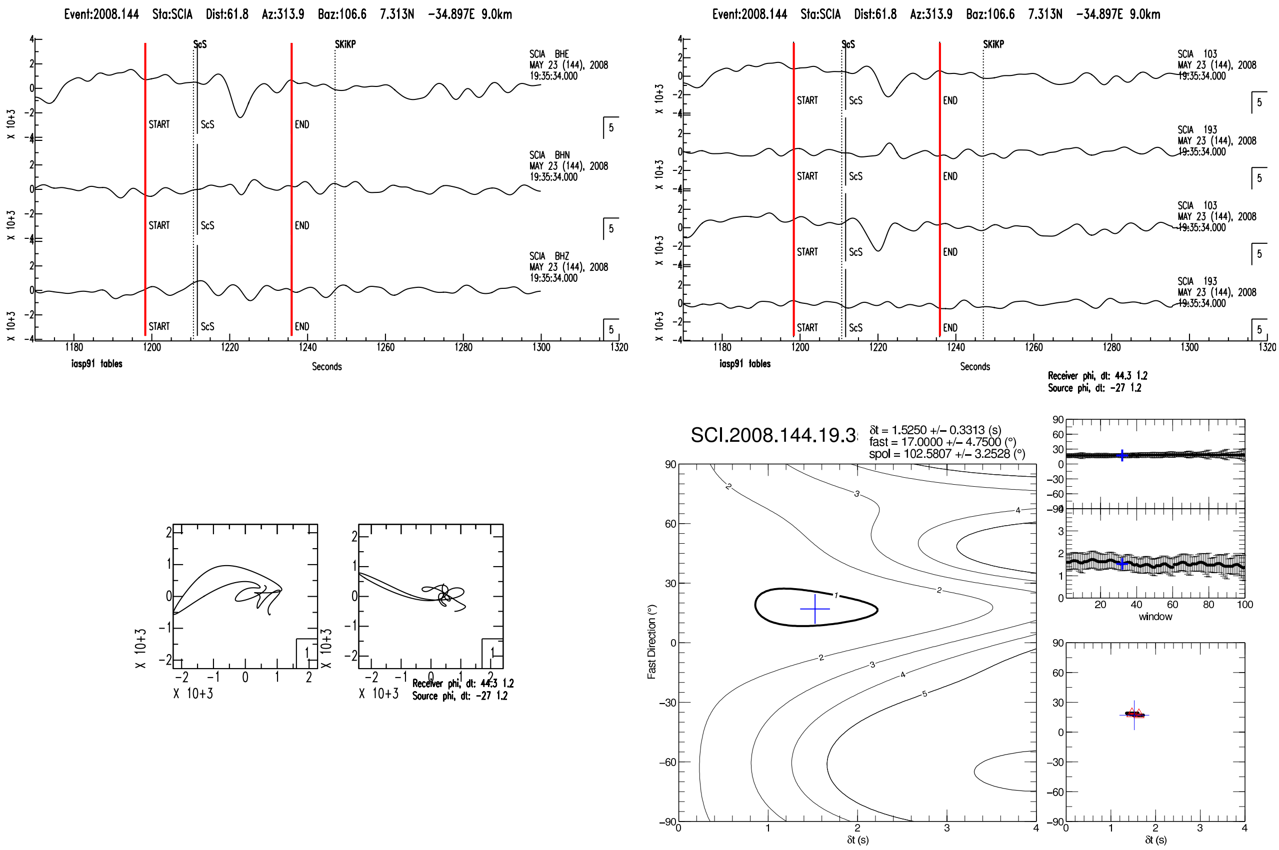

Supplementary Figure 4: Splitting analysis of ScS phase at station SCIA (State Center, Iowa, USA) from Mid-Atlantic Ridge earthquake of 2008-144-1935. Panels as described in Supplementary Fig. 3, except wavelet plots are not shown. The ScS phase is marked by the labelled solid vertical line in the upper panels. Both a receiver and source correction have been applied. Note that the transverse energy in the uncorrected waveform is removed in the corrected one, and the particle motion is linearised, indicating a good result.

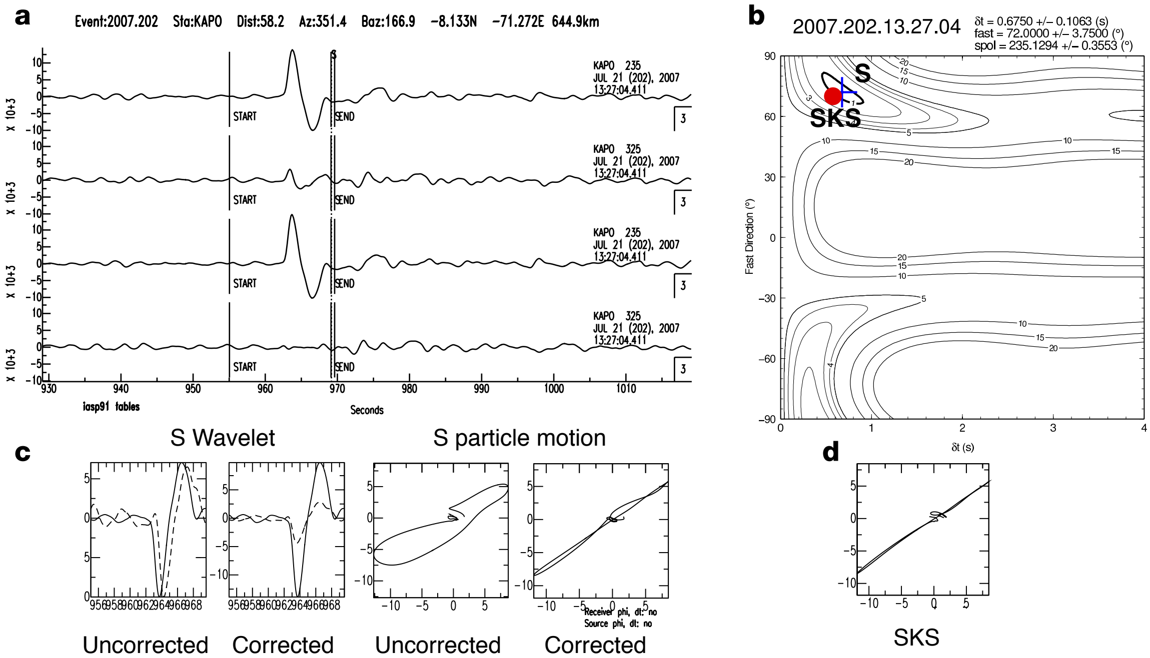

Supplementary Figure 5: Splitting analysis of uncorrected S wave from event on 2007-202-1327 (Brazil, depth 645 km) at station KAPO (Kapuskasing, Ontario, Canada), compared to SKS[10] at the same station. **a,** Uncorrected (top two traces) and corrected (bottom traces) radial and transverse components for S. The transverse energy is well removed by the measurement, which gives the parameters $\phi_{\mathrm{S}} = (72.0 \pm 3.8)^{\circ}$, $\delta t_{\mathrm{S}} = (0.67 \pm 0.11)$ s. **b,** λ_2 surface for S result. Blue cross shows optimum splitting parameters for S. Also shown is the value obtained for SKS (red dot; size is smaller than the uncertainty in the parameters), $\phi_{\mathrm{SKS}} = 69^{\circ}$, $\delta t_{\mathrm{SKS}} = 0.58$ s. They are the same within error, confirming that there is likely no source-side splitting present in the signal for such deep events. **c,** (Left to right) Wavelet plots and particle motions for respectively uncorrected and corrected split S waves. The splitting parameters linearise the particle motion well. **d,** Particle motion of the SKS phase before analysis, after applying the S splitting parameters ($\phi_{\mathrm{S}}, \delta t_{\mathrm{S}}$) as a receiver correction. As expected, using either to correct the other results in linear particle motion and no splitting (a null result), and confirms that SKS can be used as an UM correction for S.

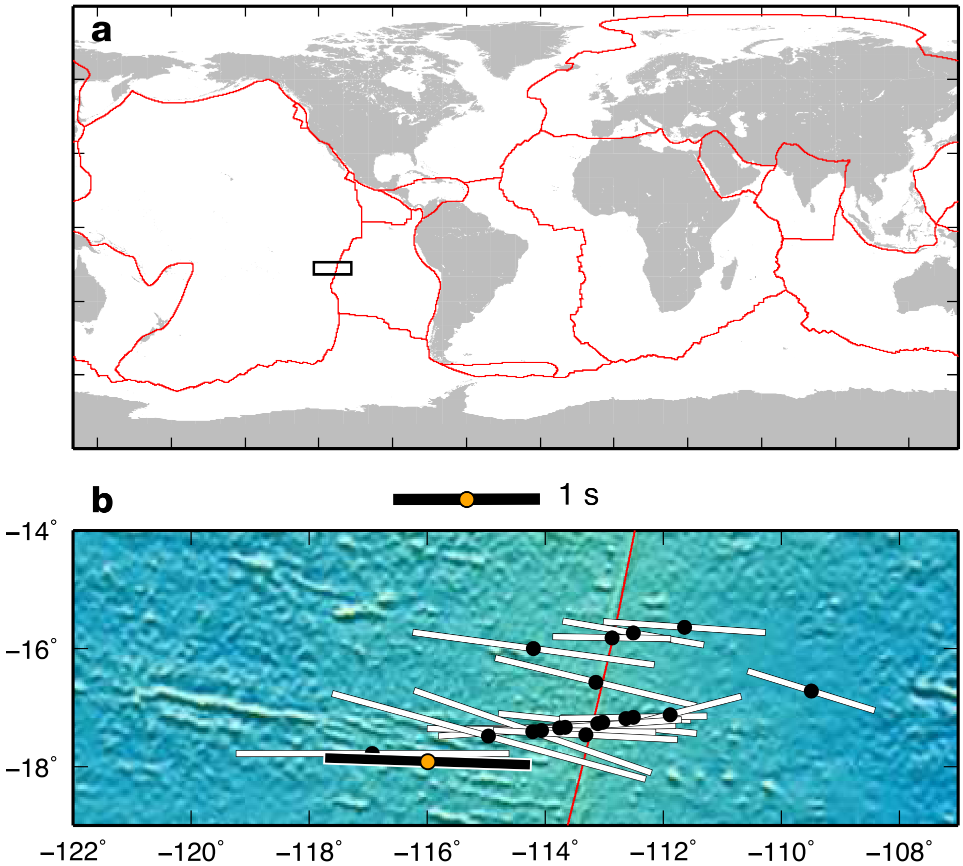

Supplementary Figure 6: SKS splitting measurements of Wolfe & Solomon[11] and source-side splitting of earthquake of 1994-246-1156 (Supplementary Table 3) calculated by analysis of direct S phase with SKS measurements used as a receiver-side correction (this study). **a,** Index map showing location of (b) on the EPR. Red lines show major plate boundaries. **b,** SKS splitting parameters made at OBSs on the EPR (white bars beneath black circles for OBS locations: angle is fast orientation; length is proportional to delay time as shown in the key, middle). Errors in ϕ_{SKS} are around 5° or more. Orange circle is location of event 1994-246-1156; black bar orientation shows ϕ''; length is proportional to δt. The measurement of source anisotropy is remarkable in its similarity to the OBS-determined UM anisotropy.

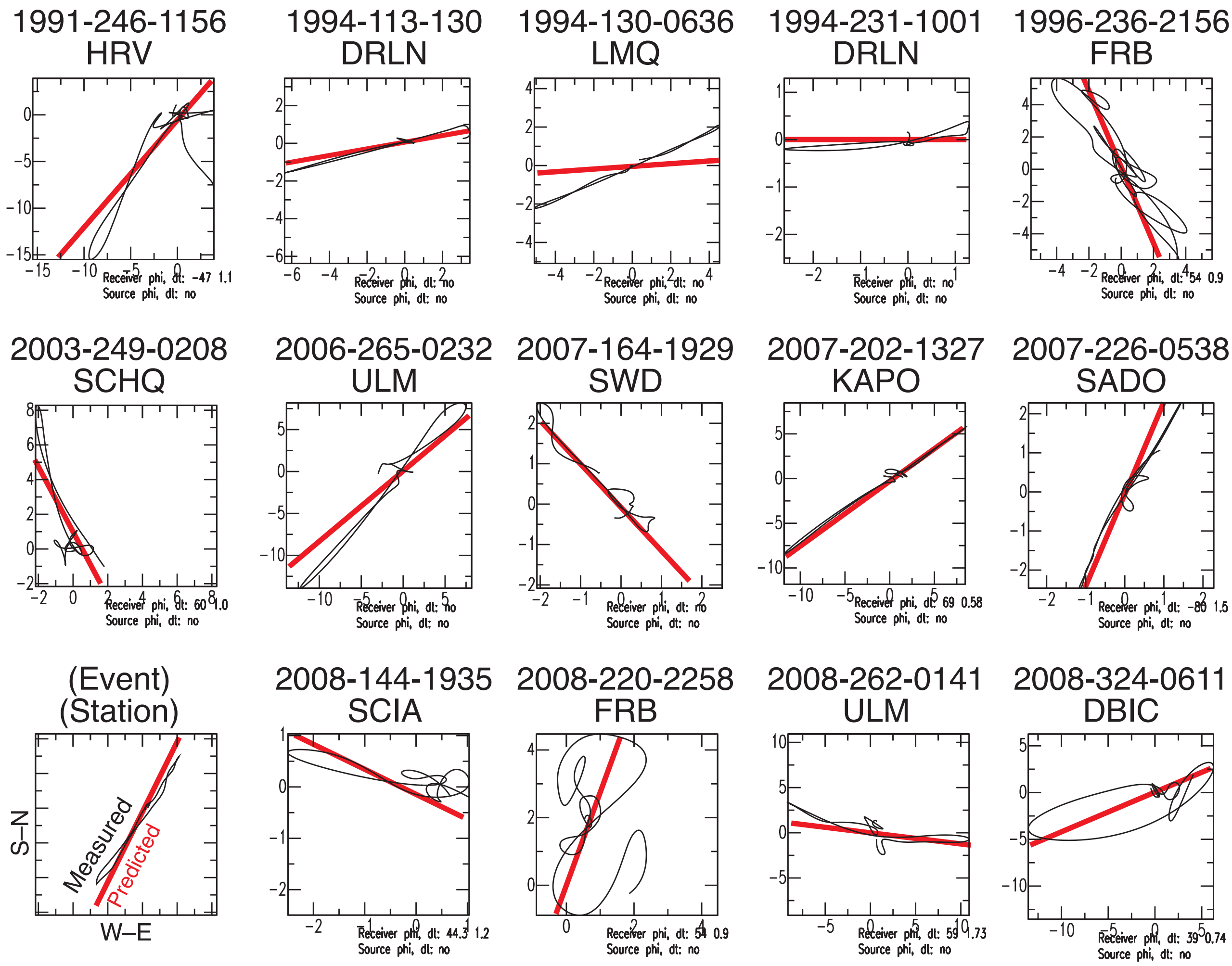

Supplementary Figure 7: Predicted and measured horizontal particle motion for each earthquake used in this study at an example station, showing the match between measured and predicted source polarisations. The measured (black) particle motions are calculated for the corrected S phase after splitting has been measured. For deep events, no source anisotropy correction is made (denoted by 'Receiver phi, dt: no' beneath the subfigure); for shallow events, an SKS correction is applied to remove the receiver UM anisotropy (given in the values beneath the subfigure). The predicted (red) particle motions are calculated using the parameters given by the Global CMT solutions for the event, giving a source polarisation that is projected onto the station.

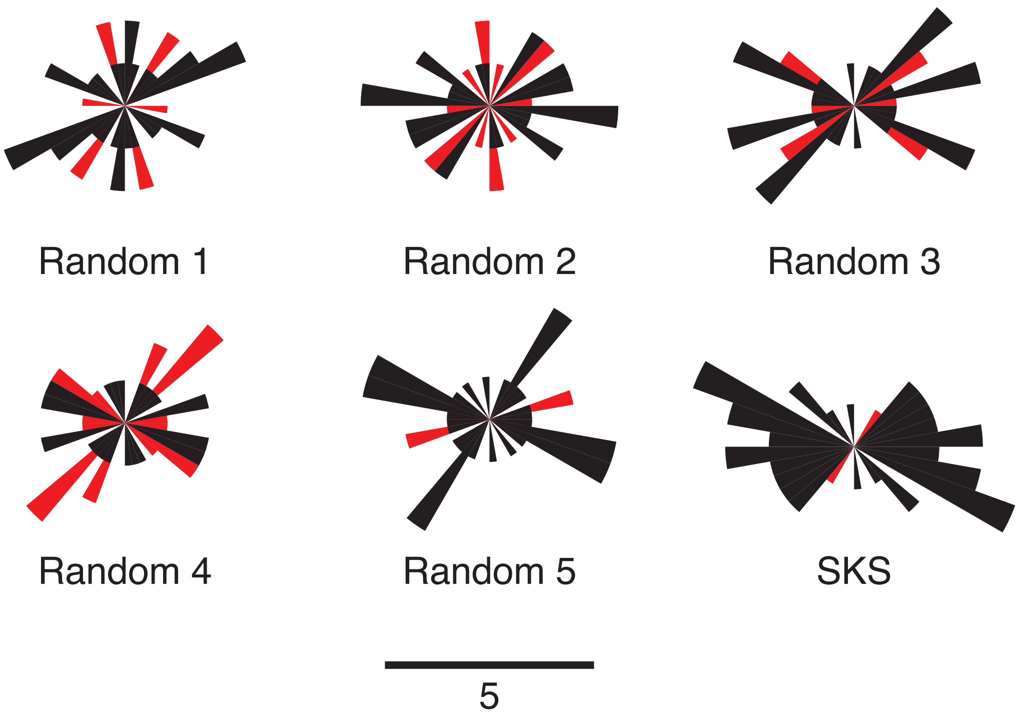

Supplementary Figure 8: Polar histograms of ϕ'' for five sets of randomised SKS 'corrections' when analysing the S phase for the MAR event of 2008-114-1935; also for the set of SKS actually used in the analyses. ϕ'' is the projection of the measured geographic fast orientation at the receiver back to the source, such that $\phi'' = \text{azimuth} + \text{backazimuth} - \phi$. Black bars show number of measurements in each 10° bin. Red bars show bins of null or very large measurements of δt. There is a 180° ambiguity in the measurements. The radial frequency axis is shown by the scale bar, bottom. We note that the number of very large or null measurements is smallest by far for the case of using real SKS measurements as receiver corrections.

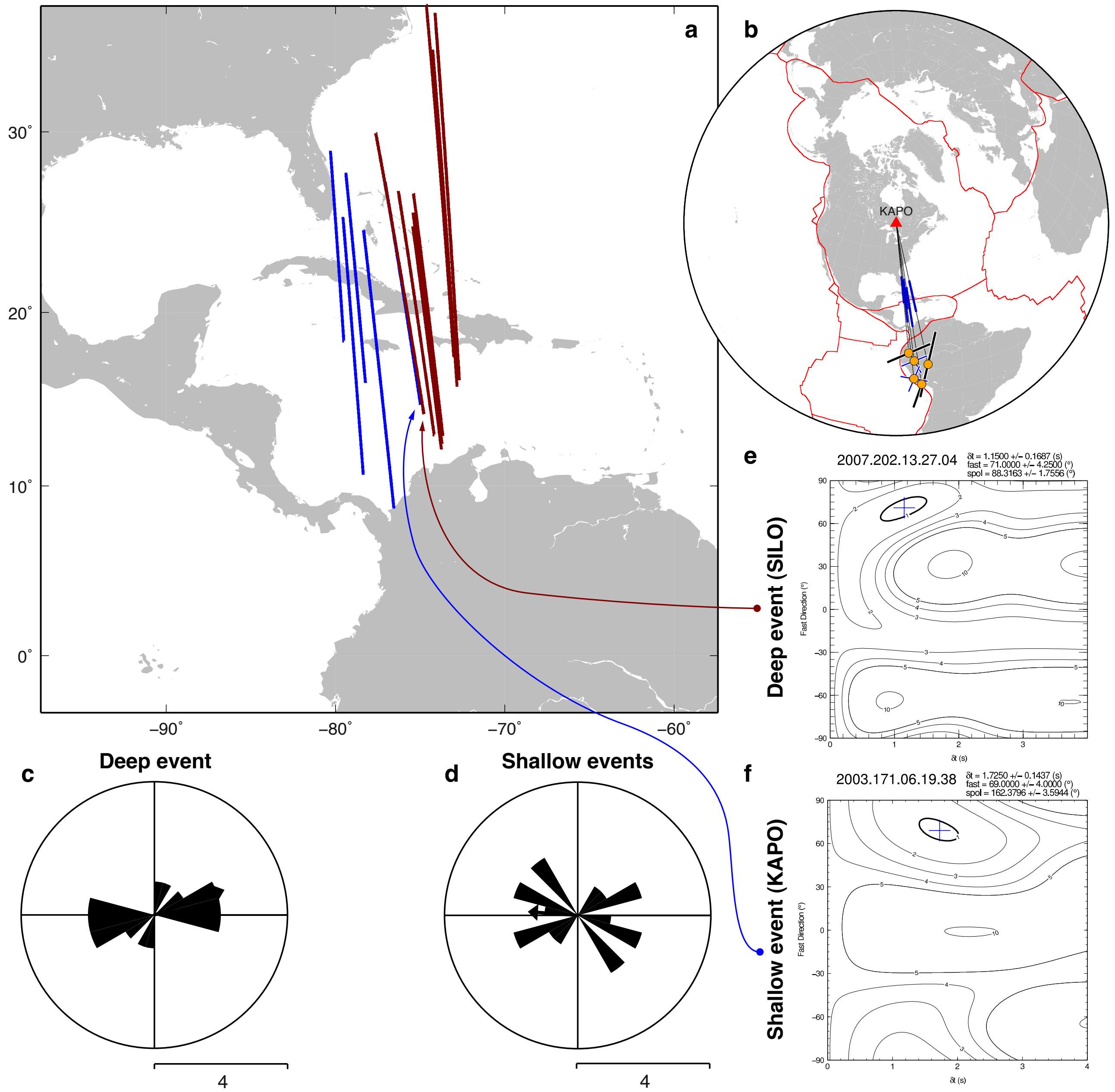

Supplementary Figure 9: Comparison between corrected ScS ϕ' from deep and shallow events. **a,** Map of ray paths in a 250 km-thick D$''$ for ray from deep (red) and shallow (blue) events. **b,** Shallow event locations with source-side UM splitting (black bars; orientation is ϕ'', length shows δt, to maxm. 3 s) and null directions (blue bars). **c and d,** polar histograms showing ϕ' for ScS for deep and shallow events respectively. Up is $\phi' = 0°$, as for Fig. 2 and Supplementary Fig. 11. The latter are recorded at KAPO. Scale bar shows radial frequency; near-null directions have been downweighted for the shallow measurements to avoid bias. **e and f,** Error (λ_2) surfaces for ϕ–δt in the geographic frame for the most closely overlapping ray paths. **e** is for the deep event recorded at SILO, **f** shows that for shallow event 2003-171-0619. The two are the same within the 95% confidence limit (thick black line).

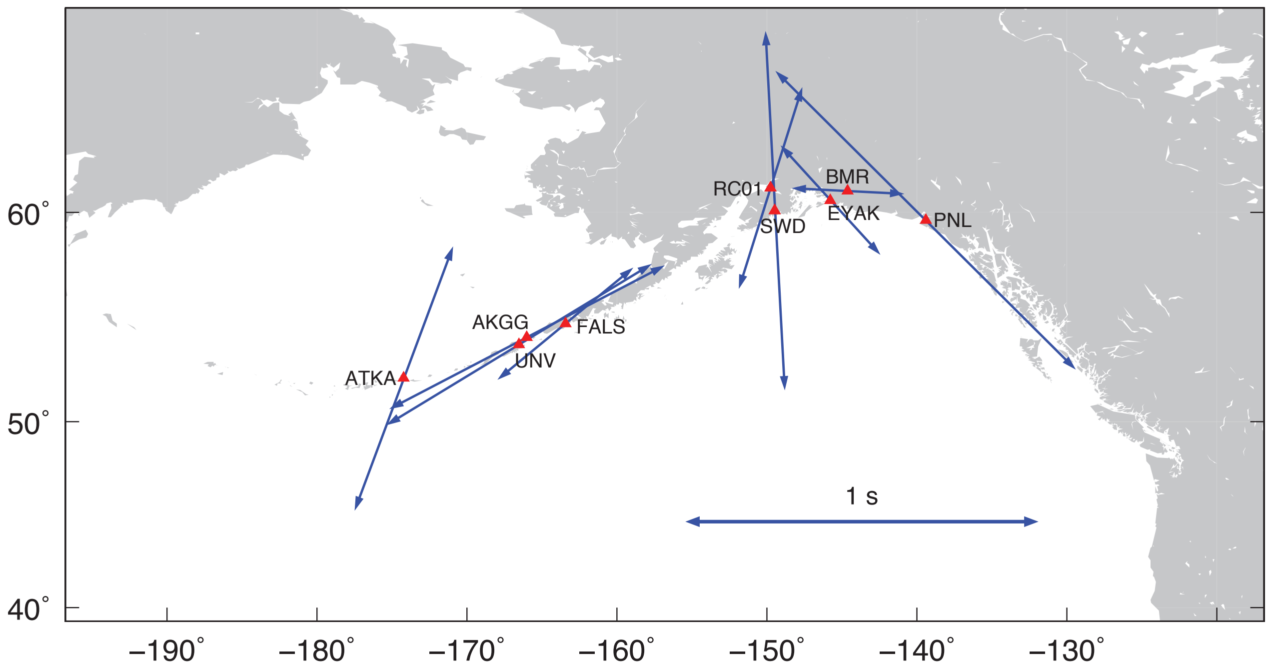

Supplementary Figure 10: Splitting parameters of SKS at stations in Alaska made in this study. For RC01 and SWD, the stacked measurements are shown. Fast direction ϕ is indicated by orientation of arrow; delay time δt is represented by arrow length according to the scale.

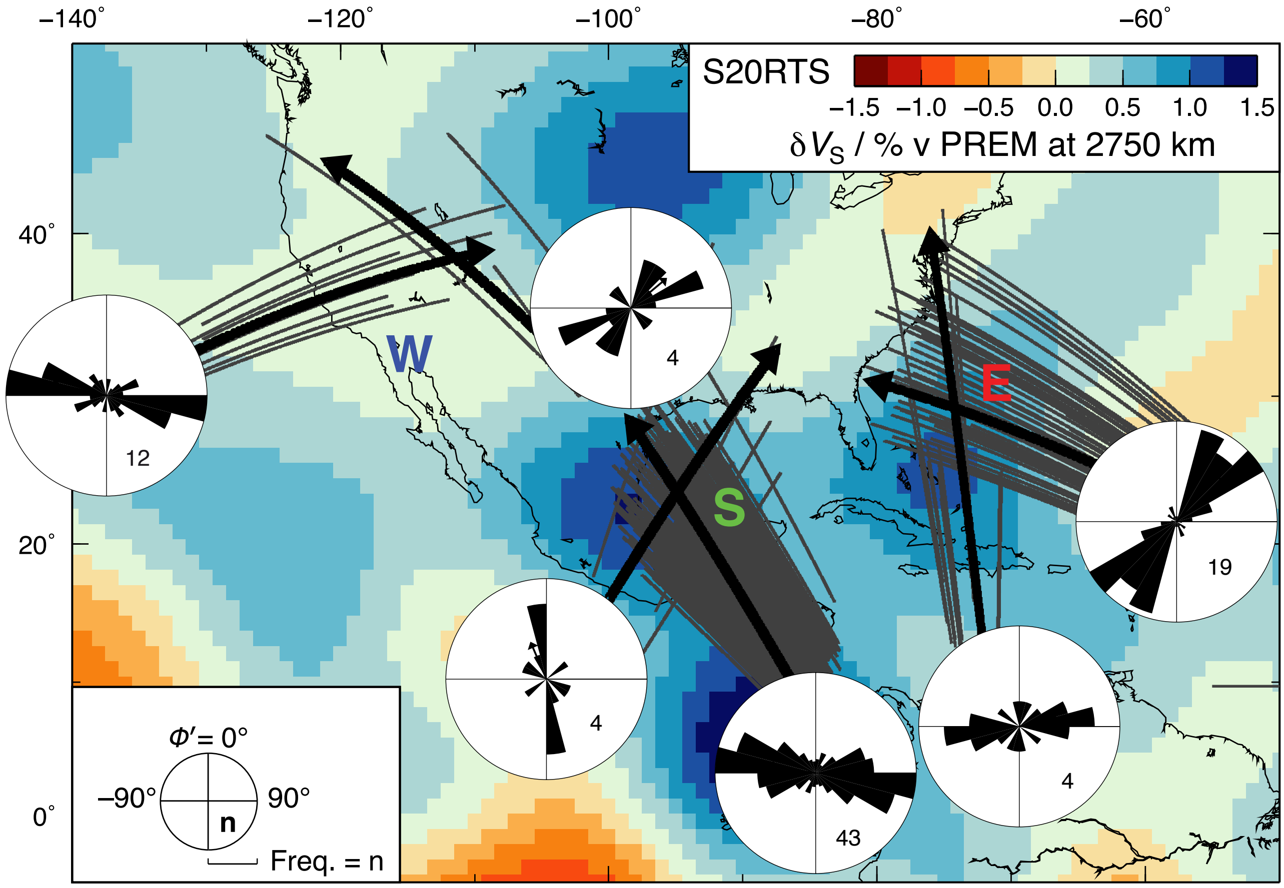

Supplementary Figure 11: Polar histograms of the ray-frame fast directions (ϕ') of individual measurements of splitting in ScS along each path. The frequency (radial) axis maximum is given by the number n in each histogram. Where visible, the black arrow gives the arithmetic mean of ϕ'. δt is not represented in this diagram. Other features as for Fig. 2.

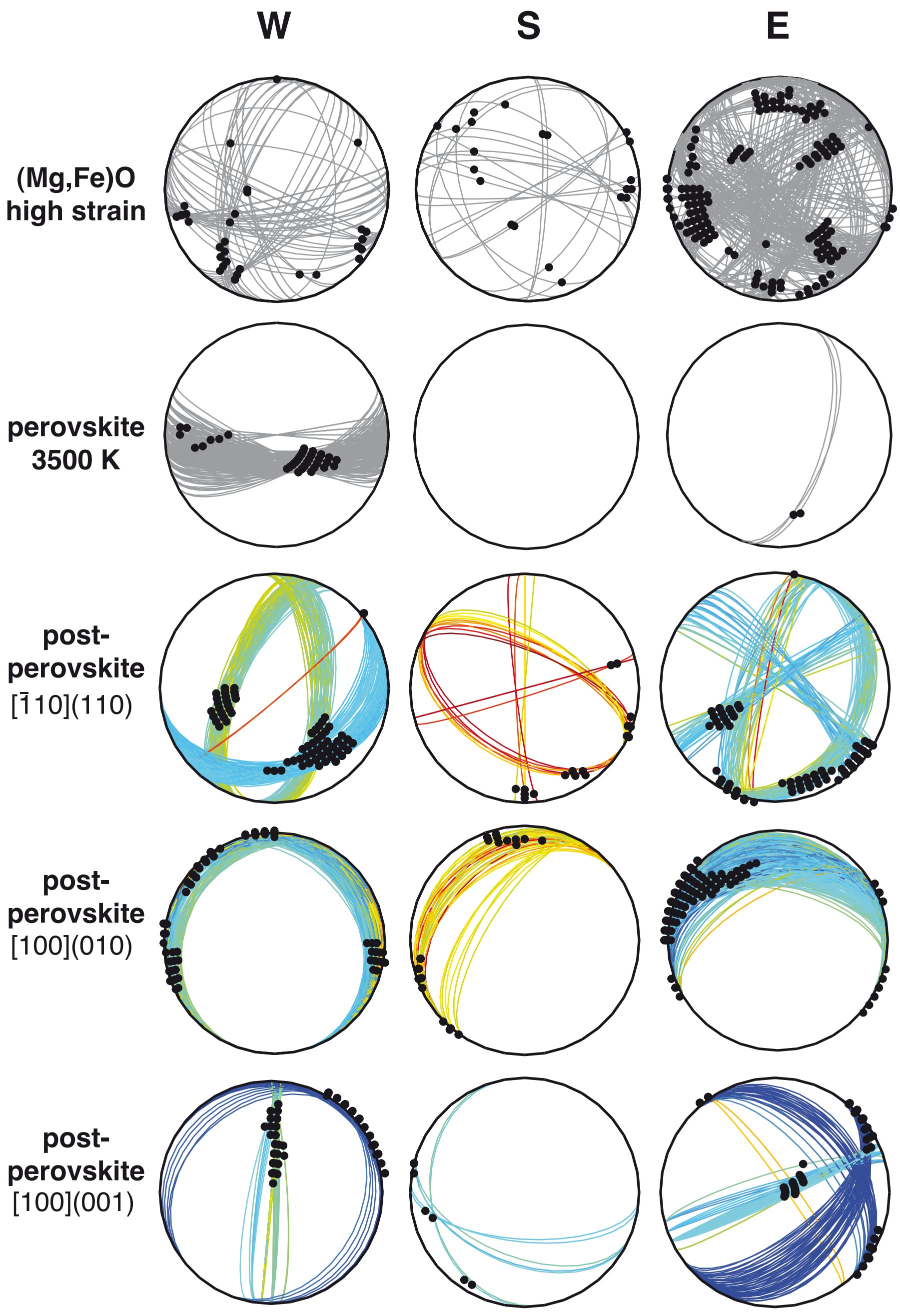

Supplementary Figure 12: Orientations of shear planes for MgO and perovskite which are compatible with our measurements of anisotropy in D″, alongside those shown in Figure 3 for post-perovskite. Equal-area upper hemisphere plots show shear planes (grey lines) and slip directions (black circles) for the expected slip systems in (Mg,Fe)O (ref. [8]) and $MgSiO_3$-perovskite (ref. [9]) which produce alignment of the mineral phase to produce anisotropy compatible with our measurements. Out of the page is the Earth radial direction, and up is north. The three regions ('W, 'S' and 'E') are labelled.

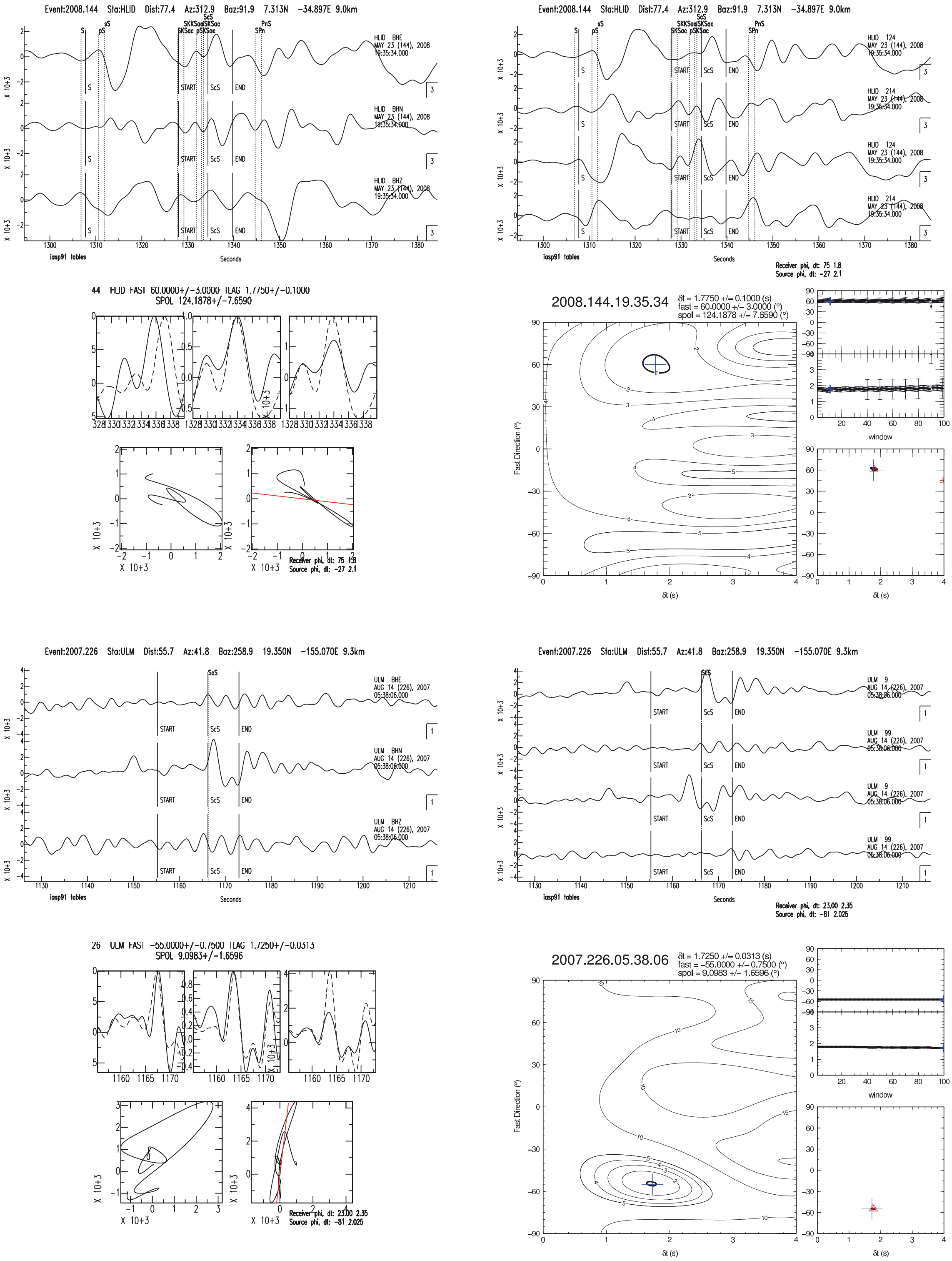

Supplementary Figure 13: Examples of differential ScS shear wave splitting measurements from a shallow earthquake. Panels are as for previous figures, with the addition of the CMT-predicted source polarisation shown in red on the corrected particle motion plots. Event and station information is given in the panels. The result in each case is very similar, particularly for ϕ.

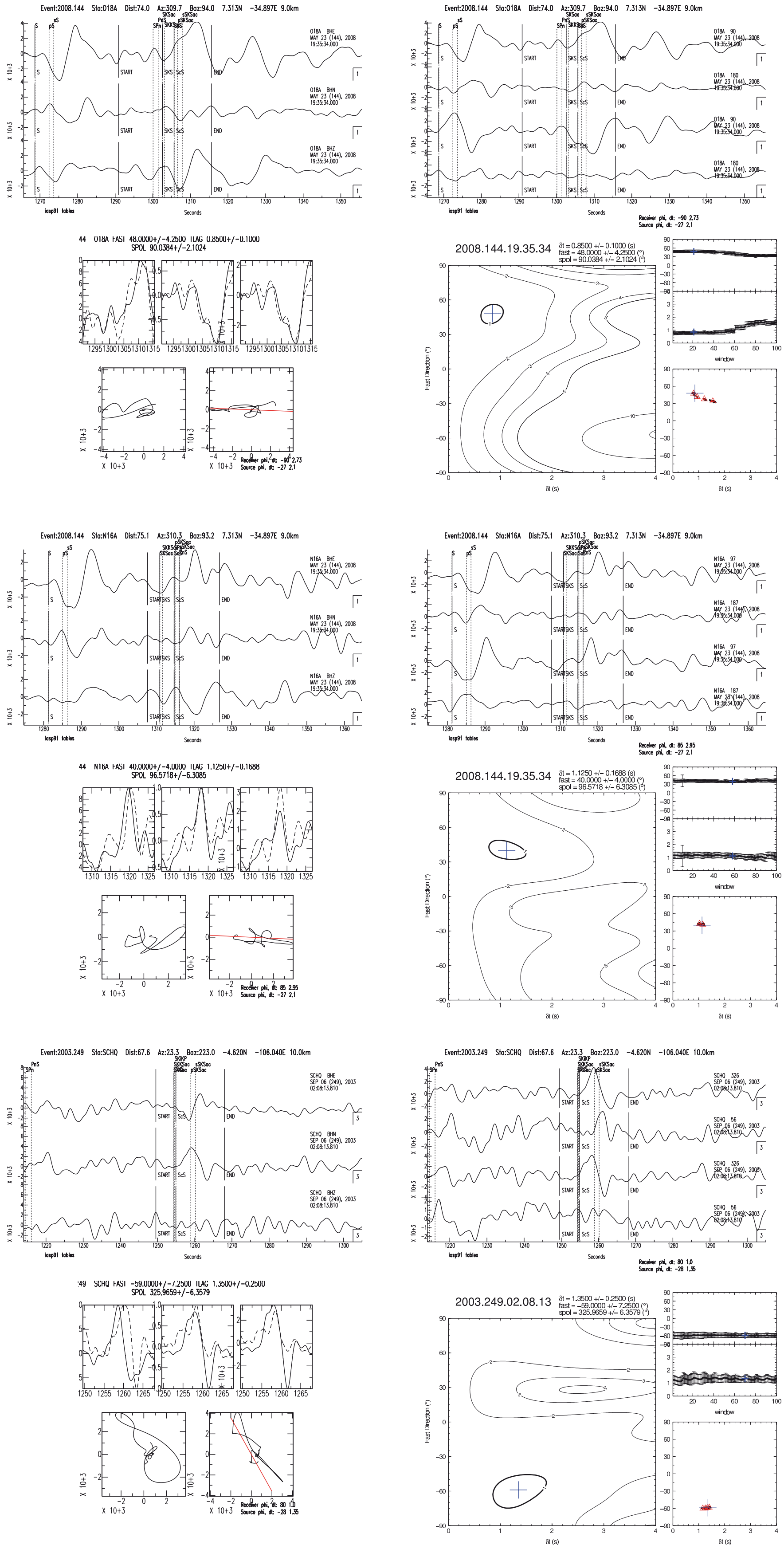

Supplementary Figure 13: (continued)

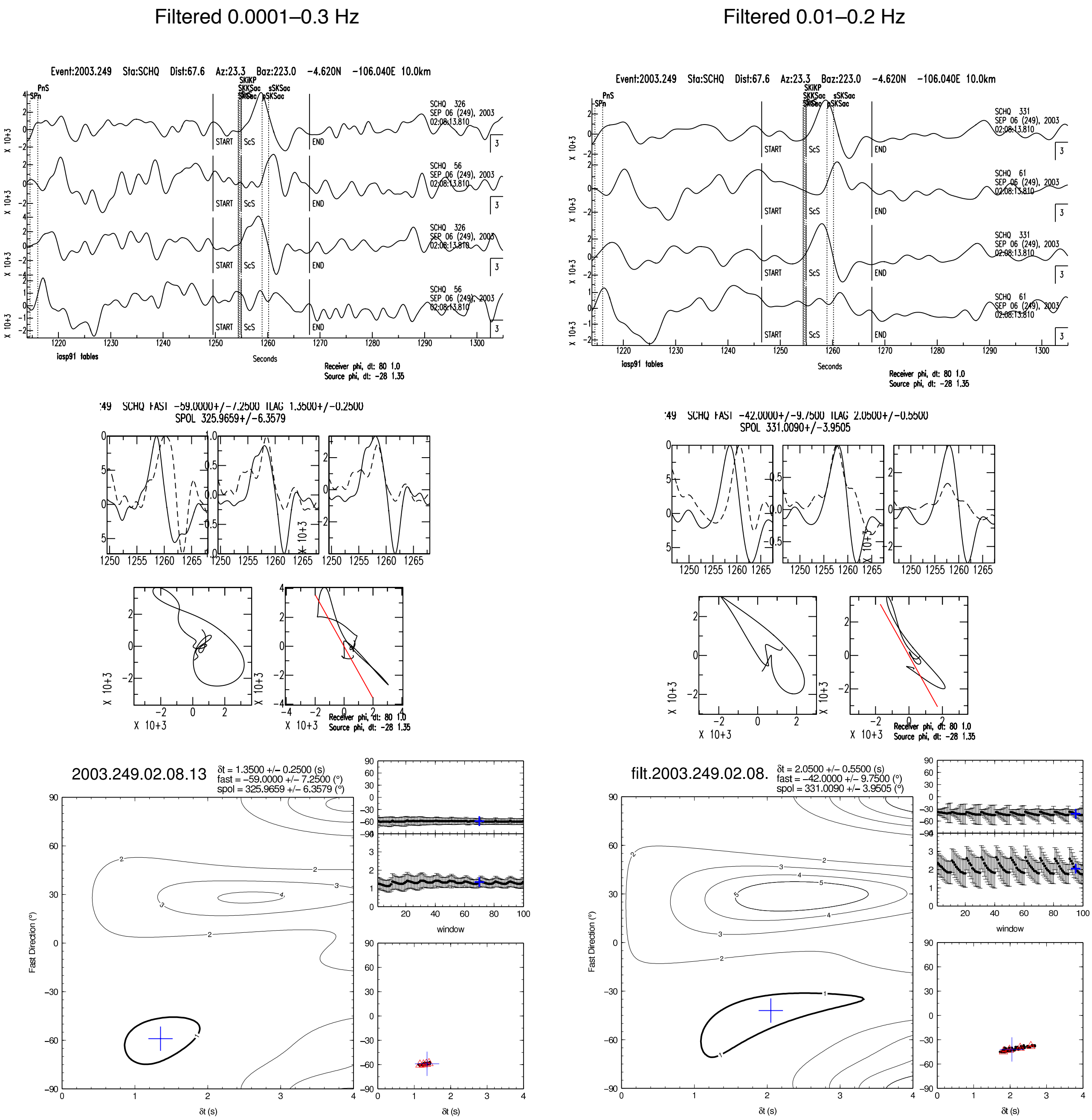

Supplementary Figure 14: Comparison of splitting results using data filtered in two different pass bands, event 2008-249-0208 recorded at SCHQ (Schefferville, Québec, Canada). The data on the left are filtered in the band 0.0001–0.3 Hz; on the right between 0.01–0.2 Hz. Although the waveforms on the right appear 'cleaner' and possibly subjectively easier to identify, the nature of the F-test used to calculate the size of the 95% confidence interval (thick black line on λ_2 surface, bottom) means that the quoted errors are larger when the frequency content of the signal is narrower. Hence we use the broader-band signal for our analyses. It is important to note that the results are the same within the 95% confidence interval in any case, which we observe to be generally true.

Supplementary Tables

Supplementary Table 1: SKS splitting measurements made in this study. Uncertainties in ϕ, $\Delta(\phi)$, and δt, $\Delta(\delta t)$ are given to the 95% confidence limit.

Station	Event (year-day-time)	Lat (°N)	Lon (°E)	Depth (km)	Backazimuth (°)	ϕ (°)	$\Delta(\phi)$ (°)	δt (s)	$\Delta(\delta t)$ (s)
AKGG	2007-202-1327	-8.13	-71.27	645	90.96	57.00	8.75	0.88	0.19
ATKA	2003-171-0637	-7.61	-71.72	560	84.82	17.00	12.00	0.80	0.07
BMR	2007-202-1327	-8.13	-71.27	645	108.45	-86.00	10.00	0.32	0.08
EYAK	2007-202-1327	-8.13	-71.27	645	107.44	-34.00	20.75	0.42	0.14
FALS	2007-202-1327	-8.13	-71.27	645	92.95	44.00	8.75	0.50	0.17
PNL	2007-202-1327	-8.13	-71.27	645	112.95	-37.00	12.25	1.20	0.24
RC01	2003-117-2314	-8.20	-71.59	560	104.28	16.00	18.25	0.50	0.56
RC01	2003-171-0636	-7.61	-71.72	560	104.11	29.00	39.50	0.68	0.99
RC01	2007-202-1327	-8.13	-71.27	645	103.97	13.00	6.75	0.60	0.13
SWD	2003-171-0636	-7.61	-71.72	560	104.37	21.00	28.75	0.85	0.88
SWD	2007-202-1327	-8.13	-71.27	645	104.24	-16.00	4.25	1.02	0.03
UNV	2007-202-1327	-8.13	-71.27	645	90.61	53.00	3.75	0.88	0.04

Supplementary Table 2: Stacked measurements of SKS at stations RC01 and SWD, used to assess the validity of nearby SKS measurements.

Station	ϕ (°)	$\Delta(\phi)$ (°)	δt (s)	$\Delta(\delta t)$ (s)
RC01	15.00	3.25	0.625	0.075
SWD	–3.00	8.75	1.050	0.313

Supplementary Table 3: Earthquakes and measured splitting parameters in S after removal of receiver-side splitting. († ϕ'' is the projection of the measured geographic fast direction at the station onto the event frame, such that $\phi'' = \text{azimuth} + \text{backazimuth} - \phi$.) Where ϕ'' is NULL, no splitting is assumed beneath the event.

Year-day-time	Locality	Lat (°N)	Lon (°E)	Depth (km)	$\phi''^\dagger$ (°)	$\Delta(\phi'')$ (°)	δt (s)	$\Delta(\delta t)$ (s)
1991-246-1156	EPR	−17.92	−115.99	11	−88	8	1.4	0.2
1994-119-0730	Argentina	−28.30	−63.25	562	NULL	-	-	-
1994-130-0636	Argentina	−28.50	−63.10	601	NULL	-	-	-
1994-231-1001	Argentina	−26.64	−63.42	564	NULL	-	-	-
1996-236-2156	EPR	−4.09	−104.37	10	25	5	2.2	0.2
2003-249-0208	EPR	−4.62	−106.04	10	82	7	1.4	0.5
2006-265-0232	Argentina	−26.77	−63.03	577	NULL	-	-	-
2007-164-1929	Guatemala	13.63	−90.73	65	−39	4	2.4	0.1
2007-202-1327	Brazil	−8.13	−71.27	645	NULL	-	-	-
2007-226-0538	Hawaii	19.35	−155.07	9	43	4	2.0	0.1
2008-144-1935	MAR	7.31	−34.90	9	73	3	2.1	0.1
2008-220-2258	EPR	−9.14	−109.52	10	81	11	2.4	0.4
2008-262-0141	EPR	−4.55	−106.00	10	90	8	1.4	0.1
2008-324-0611	Panama	8.27	−82.97	32	95	5	1.5	0.2

Supplementary Table 4: Shallow earthquakes used to compare ScS splitting parameters for deep (event 2007-202) and shallow earthquakes, measured at station KAPO.

Year-day-time	Lat (°N)	Lon (°E)	Depth (km)
2001-186-1353	−16.09	−73.99	62
2003-171-0619	−7.61	−71.72	0
2005-269-0155	−5.58	−76.39	71
2006-293-1048	−13.43	−76.57	33
2007-320-0312	−2.07	−78.20	33

Supplementary Table 5: Stacked differential S–ScS measurements made in the regions shown in Fig. 2. Azimuth is given as mean at ScS bounce point. N is number of measurements. ΔV_S, the shear wave speed variation between the fast and slow wave, is given assuming a uniform 250 km-thick D$''$ layer and the V_S model SKNA1 [12].

Region	Source	Azimuth (°)	N	ϕ' (°)	$\Delta(\phi')$ (°)	δt (s)	$\Delta(\delta t)$ (s)	ΔV_S (%)
W	Hawaii	66	17	−80	6	1.10	0.04	0.9
W	Central America	318	11	77	10	1.25	0.03	1.5
S	EPR	27	7	−42	4	1.68	0.04	1.2
S	South America	322	191	−84	3	0.90	0.01	0.8
E	South America	355	16	83	8	1.28	0.10	0.8
E	MAR	299	71	45	7	1.78	0.02	1.1

Supplementary Table 6: List of stations for which measurements are included in each of the stacked paths, for each earthquake source used.

Event	Station	Latitude	Longitude
Region W			
2007-226-0538	JCT	30.48	−99.80
2007-226-0538	NATX	31.76	−94.66
2007-226-0538	PLAL	34.98	−88.08
2007-226-0538	CNNC	35.24	−77.89
2007-226-0538	BLA	37.21	−80.42
2007-226-0538	SIUC	37.71	−89.22
2007-226-0538	CCM	38.06	−91.24
2007-226-0538	WCI	38.23	−86.29
2007-226-0538	PAL	41.01	−73.91
2007-226-0538	AAM	42.30	−83.66
2007-226-0538	NCB	43.97	−74.22
2007-226-0538	LONY	44.62	−74.58
2007-226-0538	SADO	44.77	−79.14
2007-226-0538	COWI	46.10	−89.14
2007-226-0538	EYMN	47.95	−91.50
2007-226-0538	AGMN	48.30	−95.86
2007-226-0538	ULM	50.25	−95.87
2007-164-1929	BBB	52.18	−128.11
2007-164-1929	UNV	53.85	−166.50
2007-164-1929	AKGG	54.20	−165.99
2007-164-1929	OHAK	57.22	−153.29
2007-164-1929	FIB	61.17	−150.18
2008-324-0611	BBB	52.18	−128.11

Supplementary Table 6 (continued)

Event	Station	Latitude	Longitude
Region W (continued)			
2008-324-0611	OKFG	53.41	−167.91
2008-324-0611	FALS	54.86	−163.42
2008-324-0611	PNL	59.67	−139.40
2008-324-0611	SWD	60.10	−149.45
2008-324-0611	RC01	61.09	−149.74
Region S			
1991-246-1156	HRV	42.51	−71.56
1996-236-2156	HRV	42.51	−71.56
2003-249-0208	SCHQ	54.83	−66.83
2008-220-2258	FRB	63.75	−68.55
2008-262-0141	KGNO	44.23	−76.49
2008-262-0141	LMQ	47.55	−70.33
2008-262-0141	ULM	50.25	−95.87
2007-202-1327	LLLB	50.61	−121.88
2007-202-1327	214A	31.96	−112.81
2007-202-1327	219A	32.00	−109.26
2007-202-1327	216A	32.00	−111.46
2007-202-1327	117A	32.57	−110.74
2007-202-1327	118A	32.64	−109.97
2007-202-1327	115A	32.70	−112.23
2007-202-1327	119A	32.77	−109.30
2007-202-1327	109C	32.89	−117.11
2007-202-1327	SCI2	32.98	−118.55
2007-202-1327	Z19A	33.29	−109.27
2007-202-1327	Z17A	33.30	−110.47

Supplementary Table 6 (continued)

Event	Station	Latitude	Longitude
Region S (continued)			
2007-202-1327	Z14A	33.36	−112.95
2007-202-1327	MUR	33.60	−117.20
2007-202-1327	FMP	33.71	−118.29
2007-202-1327	Y12C	33.75	−114.52
2007-202-1327	Y18A	33.78	−110.03
2007-202-1327	Y13A	33.81	−113.83
2007-202-1327	Y14A	33.94	−113.00
2007-202-1327	Y15A	33.95	−112.33
2007-202-1327	BBR	34.26	−116.92
2007-202-1327	X16A	34.42	−111.44
2007-202-1327	X19A	34.43	−109.29
2007-202-1327	X14A	34.47	−112.89
2007-202-1327	X18A	34.53	−109.95
2007-202-1327	X13A	34.59	−113.83
2007-202-1327	HEC	34.83	−116.33
2007-202-1327	RRX	34.88	−117.00
2007-202-1327	EDW2	34.88	−117.99
2007-202-1327	MPP	34.89	−119.81
2007-202-1327	W17A	35.08	−110.71
2007-202-1327	W13A	35.10	−113.89
2007-202-1327	W19A	35.11	−109.39
2007-202-1327	ARV	35.13	−118.83
2007-202-1327	W15A	35.18	−112.27
2007-202-1327	W14A	35.21	−113.08
2007-202-1327	GSC	35.30	−116.81

Supplementary Table 6 (continued)

Event	Station	Latitude	Longitude
Region S (continued)			
2007-202-1327	TUQ	35.44	−115.92
2007-202-1327	LRL	35.48	−117.68
2007-202-1327	ISA	35.66	−118.47
2007-202-1327	V12A	35.73	−114.85
2007-202-1327	V15A	35.82	−112.17
2007-202-1327	V11A	35.84	−115.43
2007-202-1327	VES	35.84	−119.08
2007-202-1327	V13A	35.85	−113.98
2007-202-1327	SHO	35.90	−116.28
2007-202-1327	PKD	35.95	−120.54
2007-202-1327	MPM	36.06	−117.49
2007-202-1327	U16A	36.14	−111.13
2007-202-1327	U04C	36.36	−120.78
2007-202-1327	HAST	36.39	−121.55
2007-202-1327	U14A	36.42	−113.18
2007-202-1327	U13A	36.42	−113.97
2007-202-1327	U11A	36.42	−115.38
2007-202-1327	U12A	36.43	−114.54
2007-202-1327	FUR	36.47	−116.86
2007-202-1327	U17A	36.60	−110.66
2007-202-1327	HELL	36.68	−119.02
2007-202-1327	T12A	36.73	−114.71
2007-202-1327	TPNV	36.95	−116.25
2007-202-1327	T16A	36.98	−111.51
2007-202-1327	GRA	37.00	−117.37

Supplementary Table 6 (continued)

Event	Station	Latitude	Longitude
Region S (continued)			
2007-202-1327	T15A	37.02	−112.38
2007-202-1327	TIN	37.05	−118.23
2007-202-1327	T14A	37.06	−113.08
2007-202-1327	T18A	37.14	−109.87
2007-202-1327	KCC	37.32	−119.32
2007-202-1327	S05C	37.35	−120.33
2007-202-1327	JRSC	37.40	−122.24
2007-202-1327	S08C	37.50	−118.17
2007-202-1327	MLAC	37.63	−118.84
2007-202-1327	S18A	37.69	−109.99
2007-202-1327	S09A	37.72	−117.22
2007-202-1327	S19A	37.75	−109.14
2007-202-1327	S14A	37.76	−113.17
2007-202-1327	S06C	37.88	−119.85
2007-202-1327	R15A	38.21	−112.28
2007-202-1327	R09A	38.24	−117.07
2007-202-1327	R04C	38.26	−120.94
2007-202-1327	R19A	38.29	−109.26
2007-202-1327	R11A	38.35	−115.59
2007-202-1327	R17A	38.42	−110.71
2007-202-1327	NV31	38.43	−118.15
2007-202-1327	R05C	38.70	−120.08
2007-202-1327	Q04C	38.84	−121.38
2007-202-1327	Q11A	38.85	−115.65
2007-202-1327	Q08A	38.86	−117.93

Supplementary Table 6 (continued)

Event	Station	Latitude	Longitude
Region S (continued)			
2007-202-1327	Q16A	38.92	−111.17
2007-202-1327	Q19A	38.96	−109.26
2007-202-1327	Q13A	38.96	−114.02
2007-202-1327	Q14A	38.99	−113.28
2007-202-1327	HOPS	38.99	−123.07
2007-202-1327	Q15A	39.00	−112.38
2007-202-1327	Q12A	39.04	−114.83
2007-202-1327	SUTB	39.23	−121.79
2007-202-1327	WCN	39.30	−119.76
2007-202-1327	P01C	39.47	−123.34
2007-202-1327	ORV	39.55	−121.50
2007-202-1327	P14A	39.59	−113.07
2007-202-1327	O06A	40.17	−119.83
2007-202-1327	O04C	40.32	−121.09
2007-202-1327	WDC	40.58	−122.54
2007-202-1327	N10A	40.72	−116.51
2007-202-1327	N11A	40.82	−115.74
2007-202-1327	N02C	40.82	−123.31
2007-202-1327	JCC	40.82	−124.03
2007-202-1327	N14A	40.85	−113.19
2007-202-1327	N13A	40.86	−114.20
2007-202-1327	M16A	41.31	−111.63
2007-202-1327	M05C	41.36	−121.15
2007-202-1327	M09A	41.42	−117.45
2007-202-1327	M14A	41.50	−113.35

Supplementary Table 6 (continued)

Event	Station	Latitude	Longitude
Region S (continued)			
2007-202-1327	MOD	41.90	−120.30
2007-202-1327	L15A	42.00	−112.39
2007-202-1327	L16A	42.01	−111.43
2007-202-1327	L07A	42.02	−119.34
2007-202-1327	L14A	42.03	−113.24
2007-202-1327	L10A	42.08	−116.47
2007-202-1327	L13A	42.09	−113.94
2007-202-1327	L12A	42.15	−115.02
2007-202-1327	WVOR	42.43	−118.64
2007-202-1327	K14A	42.55	−113.18
2007-202-1327	K07A	42.69	−119.25
2007-202-1327	K09A	42.70	−117.73
2007-202-1327	PD31	42.77	−109.56
2007-202-1327	K02A	42.77	−123.49
2007-202-1327	K10A	42.78	−116.87
2007-202-1327	K06A	42.80	−120.25
2007-202-1327	K01A	42.81	−124.47
2007-202-1327	J06A	43.25	−120.15
2007-202-1327	J09A	43.35	−117.75
2007-202-1327	J08A	43.36	−118.47
2007-202-1327	J03A	43.37	−122.96
2007-202-1327	J13A	43.40	−114.17
2007-202-1327	J11A	43.42	−115.83
2007-202-1327	J10A	43.43	−116.77
2007-202-1327	HLID	43.56	−114.41

Supplementary Table 6 (continued)

Event	Station	Latitude	Longitude
Region S (continued)			
2007-202-1327	I04A	43.79	−122.41
2007-202-1327	I13A	43.91	−114.12
2007-202-1327	I11A	43.91	−115.96
2007-202-1327	I09A	43.97	−117.74
2007-202-1327	I02A	44.00	−123.83
2007-202-1327	I07A	44.08	−119.50
2007-202-1327	I10A	44.09	−116.80
2007-202-1327	H12A	44.55	−114.86
2007-202-1327	H13A	44.56	−114.25
2007-202-1327	H10A	44.59	−116.75
2007-202-1327	H09A	44.67	−117.66
2007-202-1327	H03A	44.68	−123.29
2007-202-1327	H06A	44.73	−120.33
2007-202-1327	G13A	45.09	−114.23
2007-202-1327	G07A	45.27	−119.67
2007-202-1327	G09A	45.28	−117.78
2007-202-1327	G03A	45.32	−123.28
2007-202-1327	G11A	45.40	−116.27
2007-202-1327	F09A	45.71	−117.91
2007-202-1327	F13A	45.79	−114.33
2007-202-1327	F15A	45.84	−112.49
2007-202-1327	F07A	45.90	−119.93
2007-202-1327	F04A	45.93	−122.42
2007-202-1327	E13A	46.44	−114.19
2007-202-1327	E10A	46.49	−117.11

Supplementary Table 6 (continued)

Event	Station	Latitude	Longitude
Region S (continued)			
2007-202-1327	E08A	46.49	−119.06
2007-202-1327	E03A	46.55	−123.56
2007-202-1327	E07A	46.56	−119.85
2007-202-1327	E05A	46.56	−121.76
2007-202-1327	D15A	47.04	−112.52
2007-202-1327	D10A	47.05	−117.28
2007-202-1327	D09A	47.06	−118.31
2007-202-1327	D08A	47.06	−118.92
2007-202-1327	D14A	47.08	−113.51
2007-202-1327	D13A	47.09	−114.46
2007-202-1327	D07A	47.19	−119.97
2007-202-1327	D06A	47.19	−120.84
2007-202-1327	D05A	47.19	−121.99
2007-202-1327	C13A	47.68	−114.57
2007-202-1327	C05A	47.69	−121.69
2007-202-1327	C04A	47.72	−122.97
2007-202-1327	C14A	47.77	−113.75
2007-202-1327	C08A	47.78	−119.05
2007-202-1327	B05A	48.26	−122.10
2007-202-1327	B10A	48.30	−117.23
2007-202-1327	B09A	48.42	−118.15
2007-202-1327	B11A	48.44	−116.37
2007-202-1327	B07A	48.46	−120.12
2007-202-1327	B12A	48.47	−115.59

Supplementary Table 6 (continued)

Event	Station	Latitude	Longitude
Region S (continued)			
2007-202-1327	A04A	48.72	−122.71
2007-202-1327	A13A	48.93	−114.41
2007-202-1327	A06A	49.10	−121.48
2007-202-1327	BBB	52.18	−128.11
2007-202-1327	WHY	60.66	−134.88
Region E			
2007-202-1327	SADO	44.77	−79.14
2007-202-1327	A11	47.24	−70.20
2007-202-1327	HSMO	47.37	−79.67
2007-202-1327	A54	47.46	−70.41
2007-202-1327	A61	47.69	−70.09
2007-202-1327	TIMO	48.47	−81.30
2007-202-1327	KILO	48.50	−79.72
2007-202-1327	KAPO	49.45	−82.51
2007-202-1327	MALO	50.02	−79.76
2007-202-1327	OTRO	50.18	−81.63
2007-202-1327	SILO	54.48	−84.91
2007-202-1327	AKVQ	60.81	−78.19
2007-202-1327	IVKQ	62.42	−77.91
2007-202-1327	NOTN	63.29	−78.14
2007-202-1327	STLN	67.31	−92.98
2007-202-1327	ILON	69.37	−81.82
2008-144-1935	428A	30.73	−102.68
2008-144-1935	425A	30.79	−104.99
2008-144-1935	320A	31.34	−108.53

Supplementary Table 6 (continued)

Event	Station	Latitude	Longitude
Region E (continued)			
2008-144-1935	324A	31.44	−105.48
2008-144-1935	318A	31.44	−109.99
2008-144-1935	219A	32.00	−109.26
2008-144-1935	116A	32.56	−111.70
2008-144-1935	125A	32.66	−104.66
2008-144-1935	124A	32.70	−105.45
2008-144-1935	Y18A	33.78	−110.03
2008-144-1935	Y24A	33.93	−105.44
2008-144-1935	X19A	34.43	−109.29
2008-144-1935	X25A	34.53	−104.66
2008-144-1935	X18A	34.53	−109.95
2008-144-1935	X23A	34.58	−106.19
2008-144-1935	AMTX	34.88	−101.68
2008-144-1935	W19A	35.11	−109.39
2008-144-1935	W18A	35.12	−109.74
2008-144-1935	V26A	35.80	−103.79
2008-144-1935	V22A	35.91	−106.91
2008-144-1935	U19A	36.29	−109.21
2008-144-1935	U26A	36.39	−103.74
2008-144-1935	U15A	36.43	−112.29
2008-144-1935	U17A	36.60	−110.66
2008-144-1935	PBMO	36.78	−90.43
2008-144-1935	T19A	36.83	−109.02
2008-144-1935	T16A	36.98	−111.51
2008-144-1935	T17A	37.00	−110.80

Supplementary Table 6 (continued)

Event	Station	Latitude	Longitude
Region E (continued)			
2008-144-1935	T13A	37.02	−113.91
2008-144-1935	T18A	37.14	−109.87
2008-144-1935	S17A	37.64	−110.80
2008-144-1935	S19A	37.75	−109.14
2008-144-1935	FVM	37.98	−90.43
2008-144-1935	CCM	38.06	−91.24
2008-144-1935	R18A	38.39	−109.89
2008-144-1935	Q20A	38.95	−108.30
2008-144-1935	Q15A	39.00	−112.38
2008-144-1935	P18A	39.63	−110.25
2008-144-1935	O18A	40.27	−110.01
2008-144-1935	N16A	40.89	−111.44
2008-144-1935	N18A	40.98	−109.67
2008-144-1935	M12A	41.42	−114.92
2008-144-1935	M18A	41.43	−110.07
2008-144-1935	M17A	41.47	−110.67
2008-144-1935	M21A	41.61	−107.36
2008-144-1935	SCIA	41.91	−93.22
2008-144-1935	L18A	41.92	−110.04
2008-144-1935	L21A	41.96	−107.37
2008-144-1935	L13A	42.09	−113.94
2008-144-1935	L17A	42.10	−110.87
2008-144-1935	K17A	42.75	−110.92
2008-144-1935	PD31	42.77	−109.56
2008-144-1935	BW06	42.77	−109.56

Supplementary Table 6 (continued)

Event	Station	Latitude	Longitude
Region E (continued)			
2008-144-1935	J18A	43.21	−110.02
2008-144-1935	RRI2	43.35	−111.32
2008-144-1935	J17A	43.36	−110.71
2008-144-1935	TPAW	43.49	−110.95
2008-144-1935	HLID	43.56	−114.41
2008-144-1935	DCID1	43.59	−111.18
2008-144-1935	G16A	45.23	−111.80
2008-144-1935	COWI	46.10	−89.14
2008-144-1935	E17A	46.46	−110.86
2008-144-1935	LAO	46.69	−106.22
2008-144-1935	D16A	47.03	−111.55
2008-144-1935	C17A	47.63	−110.76
2008-144-1935	B16A	48.41	−111.71
2008-144-1935	DGMT	48.47	−104.20
2008-144-1935	ALE	82.50	−62.35
2008-144-1935	ALE	82.50	−62.35
2008-144-1935	PLCA	−40.73	−70.55
2008-324-0611	DBIC	6.67	−4.86

References

1. Wolfe, C. & Silver, P. Seismic anisotropy of oceanic upper mantle: Shear wave splitting methodologies and observations. *J Geophys Res-Sol Ea* **103**, 749–771 (1998).

2. Teanby, N., Kendall, J. M. & der Baan, M. V. Automation of shear-wave splitting measurements using cluster analysis. *B Seismol Soc Am* **94**, 453–463 (2004).

3. Dahlen, F. & Baig, A. Frechet kernels for body-wave amplitudes. *Geophys J Int* **150**, 440–466 (2002).

4. Catalli, K., Shim, S.-H. & Prakapenka, V. Thickness and Clapeyron slope of the post-perovskite boundary. *Nature* **462**, 782–U101 (2009).

5. Long, M. D., Xiao, X., Jiang, Z., Evans, B. & Karato, S. Lattice preferred orientation in deformed polycrystalline (Mg,Fe)O and implications for seismic anisotropy in D$''$. *Phys. Earth Planet. Inter.* **156**, 75–88 (2006).

6. Murakami, M., Ohishi, Y., Hirao, N. & Hirose, K. Elasticity of MgO to 130 GPa: Implications for lower mantle mineralogy. *Earth Planet Sci Lett* **277**, 123–129 (2009).

7. Karki, B., Wentzcovitch, R., de Gironcoli, S. & Baroni, S. First-principles determination of elastic anisotropy and wave velocities of MgO at lower mantle conditions. *Science* **286**, 1705–1707 (1999).

8. Yamazaki, D. & Karato, S. Fabric development in (Mg,Fe)O during large strain, shear deformation: implications for seismic anisotropy in Earth's lower mantle. *Phys. Earth Planet. Inter.* **131**, 251–267 (2002).

9. Mainprice, D., Tommasi, A., Ferre, D., Carrez, P. & Cordier, P. Predicted glide systems and crystal preferred orientations of polycrystalline silicate Mg-perovskite at high pressure: Implications for the seismic anisotropy in the lower mantle. *Earth and Planetary Science Letters* **271**, 135–144 (2008).

10. Frederiksen, A. W. *et al.* Lithospheric variations across the Superior Province, Ontario, Canada: Evidence from tomography and shear wave splitting. *J Geophys Res-Sol Ea* **112**, B07318 (2007).

11. Wolfe, C. & Solomon, S. Shear-wave splitting and implications for mantle flow beneath the MELT region of the East Pacific Rise. *Science* **280**, 1230–1232 (1998).

12. Kendall, J. M. & Nangini, C. Lateral variations in D$''$ below the Caribbean. *Geophys Res Lett* **23**, 399–402 (1996).